Failure mode of laser welds in lap-shear specimens of high strength low alloy (HSLA) steel sheets

K. ASIM, J. LEE and J. PAN

Mechanical Engineering, The University of Michigan, Ann Arbor, Michigan 48109, USA

ABSTRACT   In this paper, the failure mode of laser welds in lap-shear specimens of non-galvanized SAE J2340 300Y high strength low alloy steel sheets under quasi-static loading conditions is examined based on experimental observations and finite element analyses. Laser welded lap-shear specimens with reduced cross sections were made. Optical micrographs of the cross sections of the welds in the specimens before and after tests are examined to understand the microstructure and failure mode of the welds. Micro-hardness tests were also conducted to provide an assessment of the mechanical properties in the base metal, heat-affected and fusion zones. The micrographs indicate that the weld failure appears to be initiated from the base metal near the boundary of the base metal and the heat-affected zone at a distance away from the pre-existing crack tip, and the specimens fail due to the necking/shear of the lower left load carrying sheets. Finite element analyses based on non-homogenous multi-zone material models were conducted to model the ductile necking/shear failure and to obtain the J integral solutions for the pre-existing cracks. The results of the finite element analyses are used to explain the ductile failure initiation sites and the necking/shear of the lower left load carrying sheets. The J integral solutions obtained from the finite element analyses based on the 3-zone finite element model indicate that the J integral for the pre-existing cracks at the failure loads are low compared to the fracture toughness and the specimens should fail in a plastic collapse or necking/shear mode. The effects of the sheet thickness on the failure mode were then investigated for laser welds with a fixed ratio of the weld width to the thickness. For the given non-homogenous material model, the J integral solutions appear to be scaled by the sheet thickness. With consideration of the plastic collapse failure mode and fracture initiation failure mode, a critical thickness can be obtained for the transition of the plastic collapse or necking/shear failure mode to the fracture initiation failure mode. Finally, the failure load is expressed as a function of the sheet thickness according to the governing equations based on the two failure modes. The results demonstrate that the failure mode of welds of thin sheets depends on the sheet thickness, ductility of the base metal and fracture toughness of the heat-affected zone. Therefore, failure criteria based on either the plastic collapse failure mode or the fracture initiation failure mode should be used cautiously for welds of thin sheets.

Keywords   laser weld; necking; shear failure; failure load; ductile fracture; J integral.

NOMENCLATURE b = reduced specimen width
c = length of reduced width section
ds = differential arc length
J = J integral

Correspondence: J. Pan. E-mail: jwo@umich.edu

$\bar{\mathcal{J}}$ = scaled $\mathcal{J}$ integral
$\mathcal{J}_c$ = critical $\mathcal{J}$ integral
$\bar{\mathcal{J}}_c$ = scaled critical $\mathcal{J}$ integral
L = specimen length
$\mathbf{n}$ = unit outward normal vector
n_x = x component of the normal vector $\mathbf{n}$
P = applied load
P_o = reference load
$\bar{P}$ = normalized applied load
P_f = failure load
$\bar{P}_f$ = normalized failure load
R = fillet radius for reduced width
s = length of doublers
$\mathbf{T}$ = traction vector
T_i = components of the traction vector $\mathbf{T}$
t = sheet thickness
$\mathbf{u}$ = displacement vector
u_i = components of the displacement vector $\mathbf{u}$
V = specimen overlap length
w = laser weld width
W = specimen width
Γ = arbitrary counterclockwise contour surrounding the crack tip
σ_o = base metal yield stress
σ_u = base metal tensile strength

INTRODUCTION

Laser welding has been used in the automotive and other industries. Advantages of laser welding include narrow heat-affected zone (HAZ), high penetration due to increased power density, low distortion, relatively high welding speed, potential for automation and inherent flexibility of the process. Laser welded joints have been a topic of extensive research and investigation in the past two decades. A lap joint is a common weld joint. The geometry of a lap joint provides pre-existing crack or notch tips at the edges of the weld bead. Therefore, fatigue cracks were usually observed to be initiated from the pre-existing crack or notch tips. Structures with laser welded lap joints are often subjected to cyclic loading conditions. Therefore, many research investigations[1–9] were conducted on the fatigue lives of laser welded lap joints. However, limited research investigations were conducted on the strength of laser welded lap joints under quasi-static loading conditions. Quasi-static tests were mostly carried out in conjunction with the fatigue testing of laser welded lap joints.

Ono *et al.*[10] investigated the static and fatigue strengths of laser welded lap joints in thin steel sheets and correlated the static strength of laser welded lap joints with the tensile strength of the base metal and the hardness values of the weld. Kaitanov *et al.*[6] conducted experiments to determine the static and fatigue strengths of laser welded lap joints of steel sheets with different weld widths and penetration depths. They found that the weld width and pattern have significant effects on the static strength of the weld joints. Chien *et al.*[11] examined the shear failure of laser welded aluminium blanks under uniaxial and biaxial straining conditions. Taban *et al.*[12] experimentally investigated the static and fatigue strengths of laser welded butt joints of 12% Cr stainless steel plates. Casavola *et al.*[13] examined the static strength of laser welded butt joints of titanium sheets as well as their fatigue strength. They conducted a two-dimensional plane strain elastic finite element analysis to understand the stress concentration near the weld.

Recently, Lee *et al.*[14] conducted finite element analyses to investigate the failure mode of laser welded lap-shear specimens of high strength low alloy (HSLA) steel sheets based on the experimental results reported in this paper. Lee *et al.*[14] developed finite element models with consideration of different material sections for the weld and the weld bead geometry based on the micrograph of the cross section near the weld reported in this investigation. The tensile stress–plastic strain relation of the base metal obtained from uniaxial tensile tests was used to scale the stress–plastic strain curves of the material sections in the HAZ and fusion zone in the finite element models based on the results of the micro-hardness tests reported here.

The results of the finite element analyses of Lee *et al.*[14] were compared very well with the results of the experimental observations.

In this investigation, micrographs of the cross sections of laser welded lap joints were obtained before and after quasi-static tests. Micro-hardness tests were conducted to provide an assessment of the mechanical properties near the weld which has a varying material microstructure due to the welding process. Scanning electron micrographs of failed specimens were also obtained to understand the failure mechanism. The results of the finite element analyses of Lee *et al.*[14] were summarized here and compared with the experimental observations for completeness. Finite element analyses based on the non-homogenous 3-zone material model of Lee *et al.*[14] were then conducted to obtain the J integral solutions for the pre-existing cracks. The J integral solutions obtained from the finite element analyses based on the 3-zone material model can be used to explain the observed necking/shear failure mode of lap-shear specimens in the experiments. The effects of the sheet thickness on the failure mode of laser welds in lap-shear specimens were investigated for laser welds with a fixed ratio of the weld width to the thickness based on the non-homogeneous 3-zone finite element models. The J integral solutions from the finite element analyses are used to explain the failure modes of laser welds in lap-shear specimens of different thicknesses. Finally, the failure load is expressed as a function of the sheet thickness to demonstrate the use of the failure curves to determine the failure load and the failure mode of the welds.

EXPERIMENTS

Lap-shear specimen

HSLA steel sheets with a thickness of 0.93 mm were welded together using a 6 kW CO_2 laser at a welding speed of 8 m/min. Helium was used as the shielding gas with a discharge rate of 20 ℓ/min. No heat treatment was carried out after the welding process. The welded sheets were sheared into 275 mm by 27 mm strips that were used to make lap-shear specimens for the present study. These lap-shear specimens were then machined into a dog-bone–shaped profile using a CNC milling machine. The specimen geometry in general follows the guidelines of the ANSI/AWS B4.0:2007 standard for the mechanical testing of welds. The objective of the reduced width for the central portion of the specimen is to investigate the failure mechanism in the vicinity of the laser welds and to avoid the failure of the specimen due to the necking of the specimen sheets far away from the laser welds. Figures 1a and b show top and bottom views of a laser welded lap-shear specimen, respectively. As shown in these figures, the laser weld width is very narrow. The

(a)

(b)
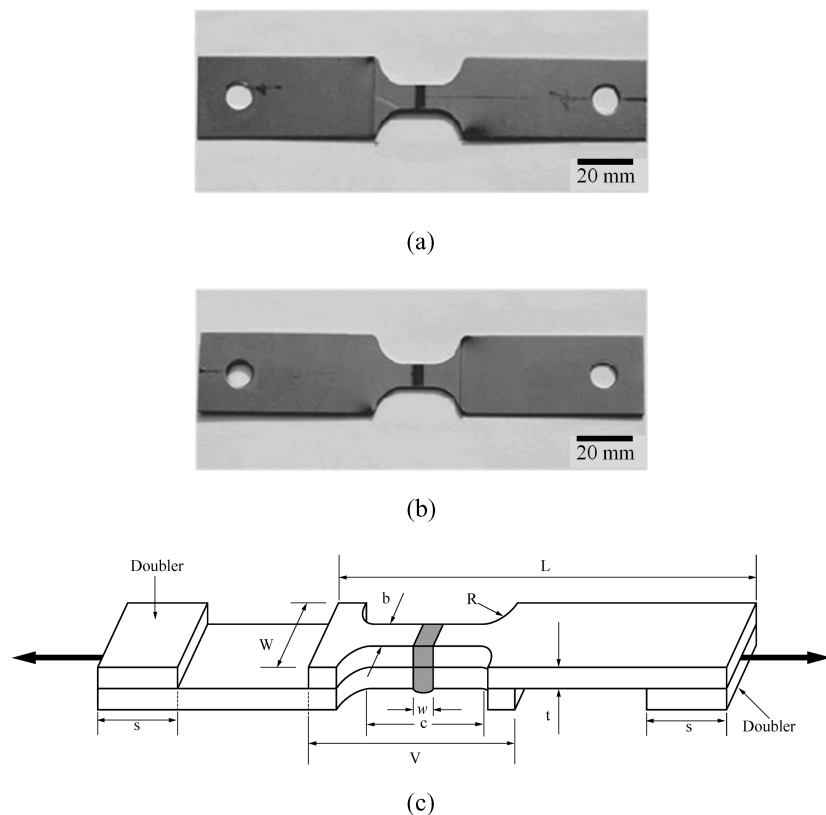
Fig. 1 (a) A top view and (b) a bottom view of a laser welded lap-shear specimen and (c) a schematic of a lap-shear specimen with the loading direction shown as the bold arrows.

(c)

Table 1 Dimensions of the lap-shear specimen

Width of the grip section (W)	27.0 mm
Width of the central portion (b)	8.0 mm
Fillet radius (R)	9.5 mm
Length of the central portion (c)	13.5 mm
Length of the doubler (s)	50.0 mm
Weld width (w)	1.0 mm
Length of each leg (L)	95.0 mm
Overlap length (V)	30.0 mm
Sheet thickness (t)	0.93 mm

average weld width was measured to be about 1 mm. The width and length of the uniform straight part for the reduced width section were measured at 8 and 13.5 mm, respectively. Specimens with similar shapes were adopted by a number of researchers for the study of laser welded joints, for example see Anand *et al.*[15] and Sripichai *et al.*[16]

Figure 1c shows a schematic of a lap-shear specimen. As shown in the figure, the specimen has a width W, sheet thickness t and overall length L for the upper and lower sheets. The specimen has a width b and a length c for the central portion of the specimen, an overlap length V and a width w for the weld zone which is indicated as the shaded area in the figure. Two doublers were used for aligning the fixtures to avoid the initial realignment of the specimen. The doubler has a length s and a width W as shown in the figure. The detailed dimensions of the lap-shear specimens are listed in Table 1. The loading direction is indicated by two bold arrows on the right and left sides of the specimen. These bold arrows are used to indicate the loading directions in the subsequent figures. After machining, the specimen edges were manually smoothed by using 1200 grit coarse polishing papers. This was done to remove notches or irregularities along the edges which may produce stress concentration sites.

Weld microstructure

The laser welded joints of the lap-shear specimens were sectioned using a low-speed diamond saw perpendicular to the welding direction. The specimens were then ground through a series of grinding steps and polished by diamond polishing compounds. The cross sections were then chemically etched to examine the microstructure of the welded area. Three per cent Nital solution was used as the etchant. Samples were etched by immersion in the etchant solution for about 20 to 30 s. Figure 2a shows an optical micrograph of the etched cross section of a laser welded joint. Three different regions can be identified from the micrograph based on their distinct grain structures, namely, the base metal, the HAZ and the fusion zone. Close-up views of the base metal, HAZ and fusion

zone are provided in Figs. 2b, c and d, respectively. The base metal has fine and randomly oriented grains.[15] The HAZ between the fusion zone and the base metal has a mixture of fine and coarse grains. The coarse grain indicates grain growth in this region due to the welding process. The span of this narrow HAZ varies from 0.05 to 0.17 mm on both sides of the fusion zone along the thickness direction. The width of the fusion zone is about 0.80 mm along the middle surface of the weld. A similar microstructural composition of the three weld zones was also reported for laser welded high strength galvanized steel sheets in Mei *et al.*[17] The micrograph in Fig. 2a also shows that the weld is free of porosities and other welding defects such as cracks and voids.

Micro-hardness test of welded joint

Micro-hardness tests were carried out using an automated CM-400AT Clark micro-hardness tester (Sun-Tec Corporation, MI, USA). All the indentations were made with a 500 g load and a dwell time of 15 s. The tests were done using a pyramidal tip to record the Vickers hardness number. The indentations were carried out at a regular interval of about 150 μm in the transverse direction across the weld zone from the base metal to the fusion zone and to the base metal on the other side. Figure 3a shows an optical micrograph of the cross section of a laser weld with micro-indentations. The hardness values from these tests are plotted in Fig. 3b for both the upper and lower sheets as well as the middle surface of the fusion zone between the pre-existing crack tips. Figure 3b shows that the hardness variations remain fairly consistent along the thickness direction. The base metal has a hardness value of less than 150 HV500. The hardness value increases sharply in the HAZ from 150 HV500 and reaches the highest value of about 230 HV500 in the fusion zone near the weld centre. The hardness values obtained from these tests were used to estimate the stress–plastic strain curves of the HAZ and fusion zone based on the stress–plastic strain curve of the base metal for the finite element analyses in Lee *et al.*[14] and the finite element analyses discussed later.

Tensile test of base metal

Tensile tests were conducted for the base metal sheets according to the ASTM E8/E8M-09 standard for tension testing of metallic materials. The HSLA sheets were cut into 200 mm rectangular specimens with a gauge length of 50 mm. The dog bone profile was made by a water-jet cutting machine. The specimen edges were manually coarse polished using 1200 grit grinding papers. The tests were carried out using an automated MTS tensile testing machine (MTS Systems Corporation, MN, USA) with a 10 kN load cell. An extensometer with a 2 inch gauge
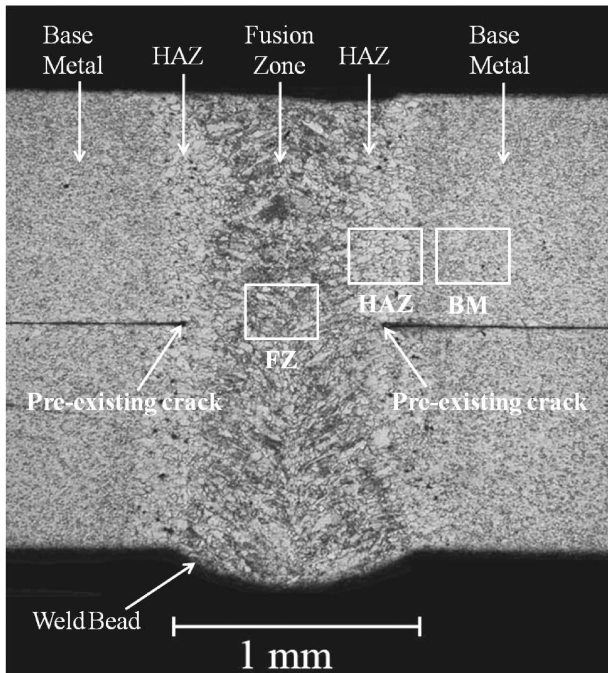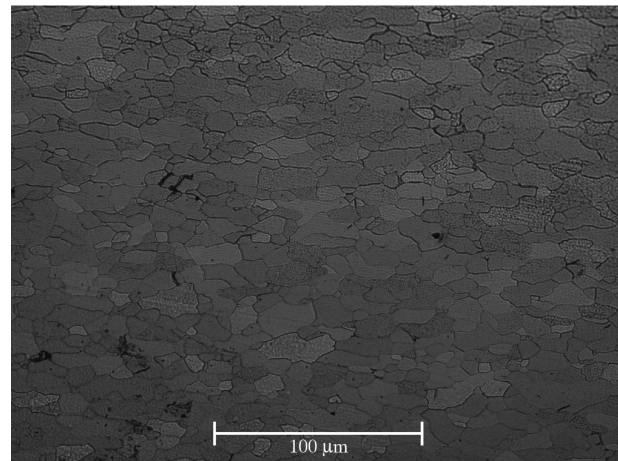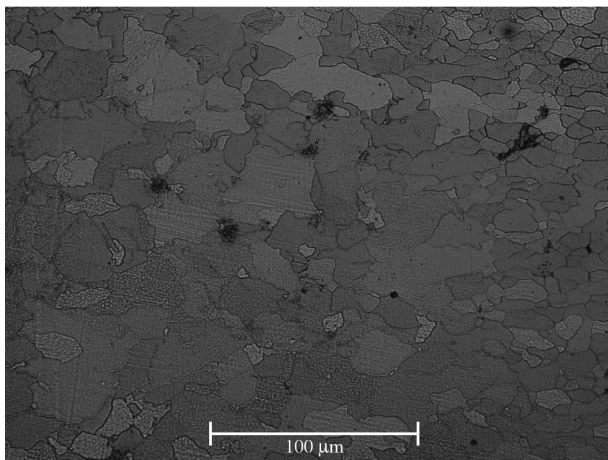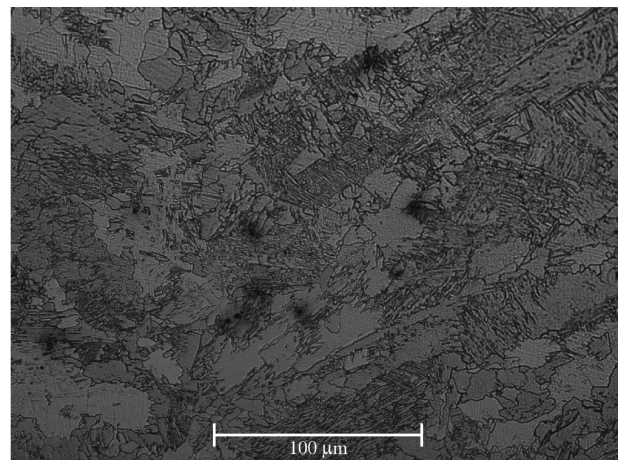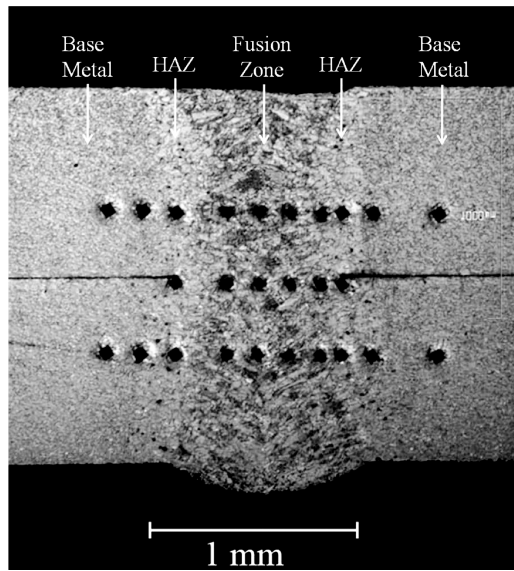
Fig. 2 (a) An optical micrograph of the etched cross section of a laser welded joint (3% Nital used as the etchant), and close-up views of (b) the base metal (BM), (c) the heat-affected zone (HAZ) and (d) the fusion zone (FZ) as marked in (a).

length was used to automatically record the extension in the uniform gauge section. The cross-head speed was maintained at 2.54 mm/min throughout the tests. The engineering stress–strain curves are shown in Fig. 4 for the base metal from three representative sheet specimens. A total of six specimens were tested. The material parameters obtained from these tests are listed in Table 2. The stress–plastic strain curves for the HAZ and fusion zone were estimated by scaling the stress–plastic strain curve of the base metal according to the hardness values of the HAZ and fusion zone.[14] These stress–plastic strain curves were used as the input parameters for the finite element analyses in Lee *et al*.[14] and the finite element analyses discussed later.

Quasi-static test of lap-shear specimen

Quasi-static tests of lap-shear specimens were carried out under displacement controlled conditions. These tests were conducted using an automated MTS testing
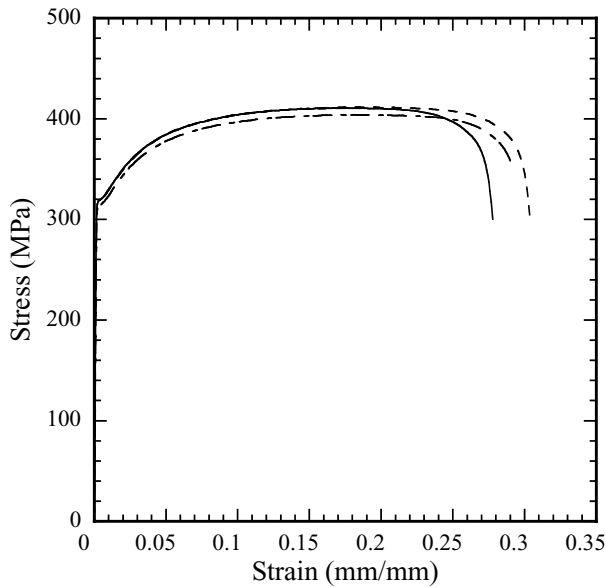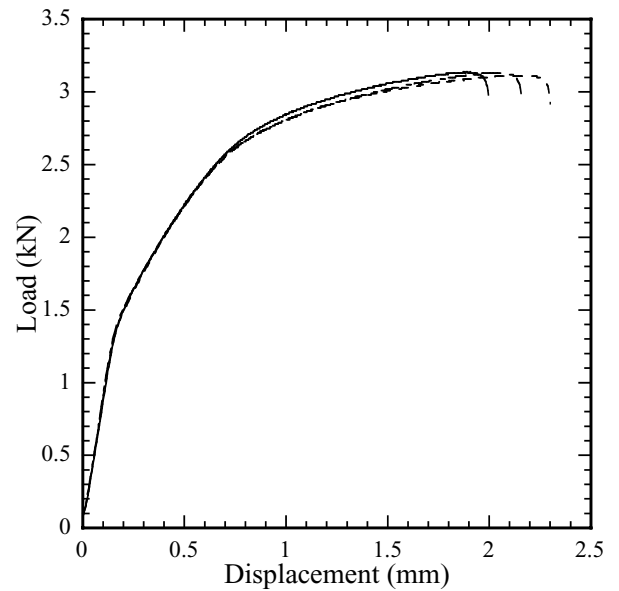
(a)
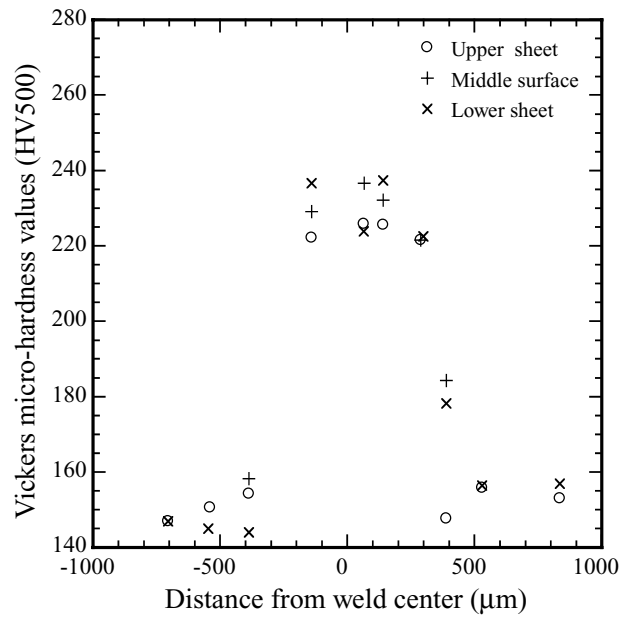
(b)

Fig. 3 (a) An optical micrograph of the cross section of a laser weld with micro-indentations and (b) the distributions of the hardness values across the weld.

**Fig. 4** The engineering stress–strain curves for the base metal from three representative sheet specimens.

Table 2 Material parameters from tensile tests of the base metal

Elastic modulus (GPa)	Yield stress (MPa)	Tensile strength (MPa)	Hardening exponent n	Strength coefficient K (MPa)
206	315	415	0.15	633

Fig. 5 The load-displacement curves from quasi-static tests of three lap-shear specimens.

machine at a constant cross-head speed of 1 mm/min. Figure 5 shows the load-displacement curves obtained from quasi-static tests of three lap-shear specimens. The average failure or maximum load and the maximum displacement obtained from these tests were about 3.1 kN and 2.16 mm, respectively. The results of these tests were used as the reference load and displacement by Sripichai

(a)

(b)

(c)

(d)
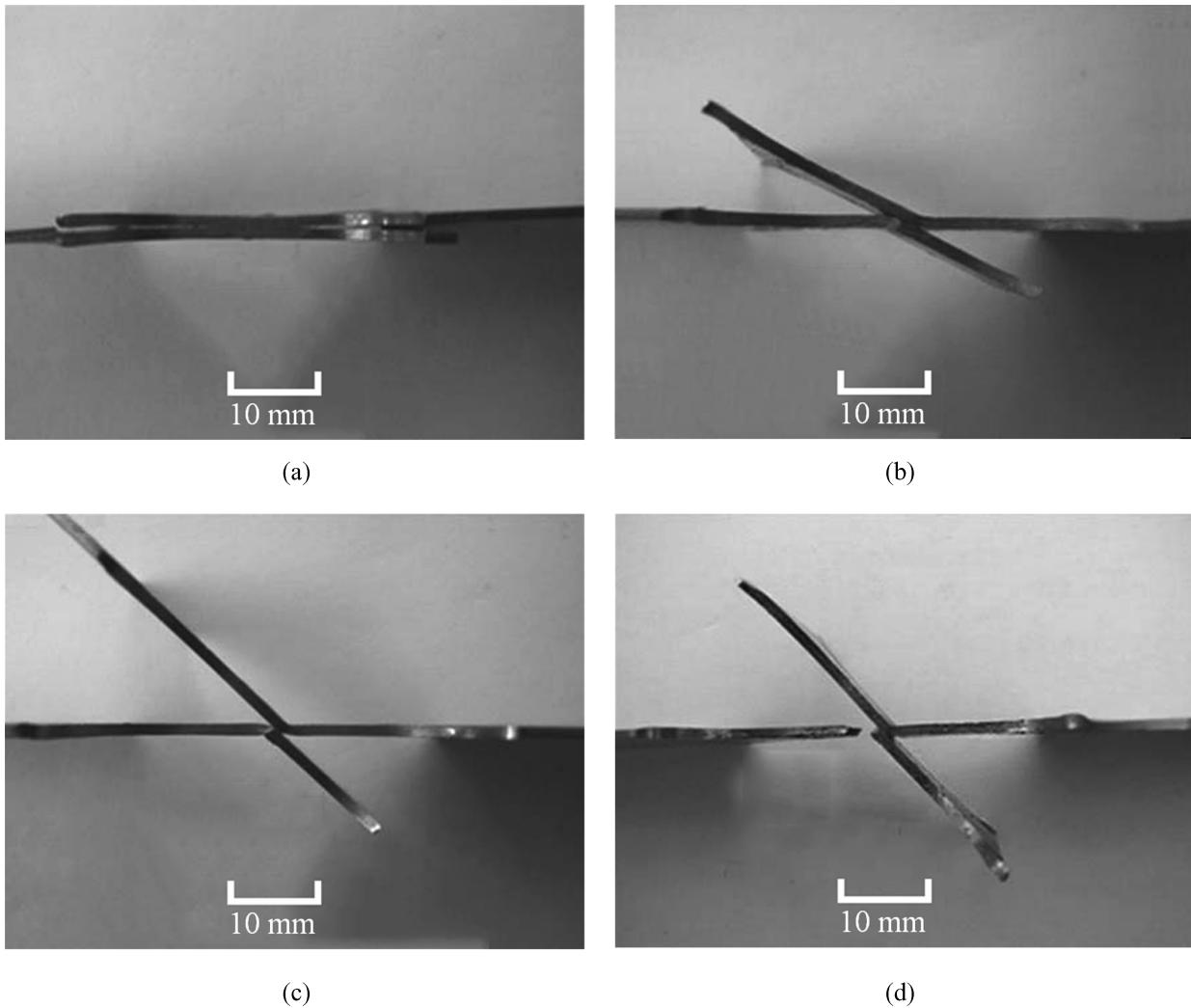
Fig. 6 Side views of specimens at the applied displacements of (a) 0.2 mm, (b) 1.0 mm, (c) 1.9 mm and (d) about 2.1 mm with the left sheet separated from the weld.

et al.[16] for fatigue testing of laser welded lap-shear specimens of HSLA steel sheets.

It was also observed during these tests that the weld bead rotated as the applied displacement increased. Figure 6 shows the side views of four specimens that had been subjected to different displacements during the quasi-static tests. Figures 6a, b and c show the side views of the specimens from the tests that were interrupted at the displacement of 0.2, 1.0 and 1.9 mm, respectively, whereas Fig. 6d shows the side view of a failed specimen at the final displacement of about 2.1 mm. The angle of rotation continued to increase throughout the tests and the final angles between 45° and 50° with respect to the load line were observed for completely failed specimens. A similar weld rotation was reported by researchers, for example in Radaj *et al.*[18] for resistance spot welds. Ono *et al.*[10] also observed the weld rotation in laser welded lap-shear specimens and

experimentally determined a maximum rotation angle of less than 25° for their specimens. The weld rotation is caused by the non-uniform plastic deformation through the thickness in the two load carrying sheets of the lap-shear specimen and by the relative rigidity of the weld bead as compared to the base metal.[14] The weld rotation is also dependent on the weld width.[14] The necking of the sheet metal near the weld zone is also somewhat visible from Fig. 6d for the separated lower left sheet after the complete failure of the laser weld. For a total of eight tests, the failure of all the specimens occurred in the lower left load carrying sheets near the weld beads.

To further study the failure mechanism in detail, the tested specimens were sectioned perpendicular to the weld direction using a low-speed diamond saw and prepared for a micrographic analysis. The sectioned specimens were ground with grinding papers of different grit size in a

series of steps to remove any cold work effects which might have been left at the sheet edges due to the machining. The specimens were then polished using diamond suspension compounds. A detailed analysis of these micrographs is presented in the following sections.

FAILURE MECHANISM OF WELDED JOINT

A micrographic analysis of nearly failed and failed laser welds under quasi-static loading conditions is presented here. Figure 7a shows an optical micrograph of the cross-section near the weld in a specimen just prior to its complete separation. The bold arrows in the figure indicate the loading direction. The upper right and lower left sheets were the two load carrying sheets in these tests. The necking of the upper right and lower left sheets can be observed. A crack formation at a distance away from
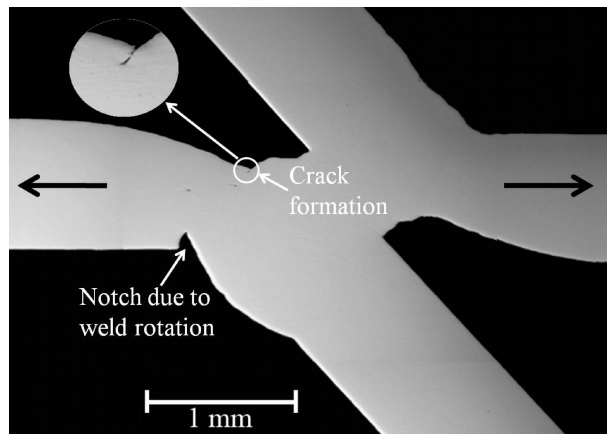
(a)
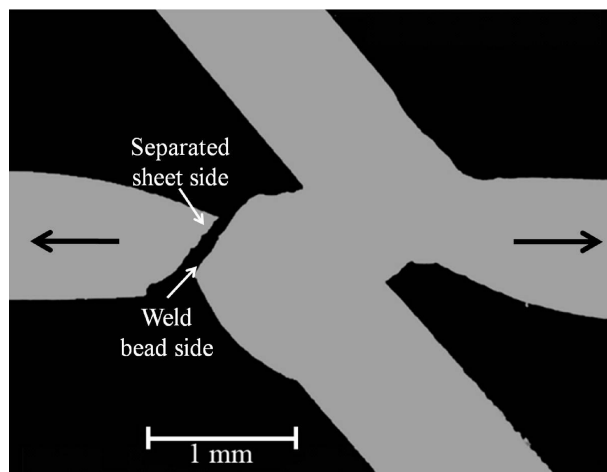
(b)

Fig. 7 Optical micrographs of the cross sections of the weld for (a) a nearly failed and (b) a failed weld.
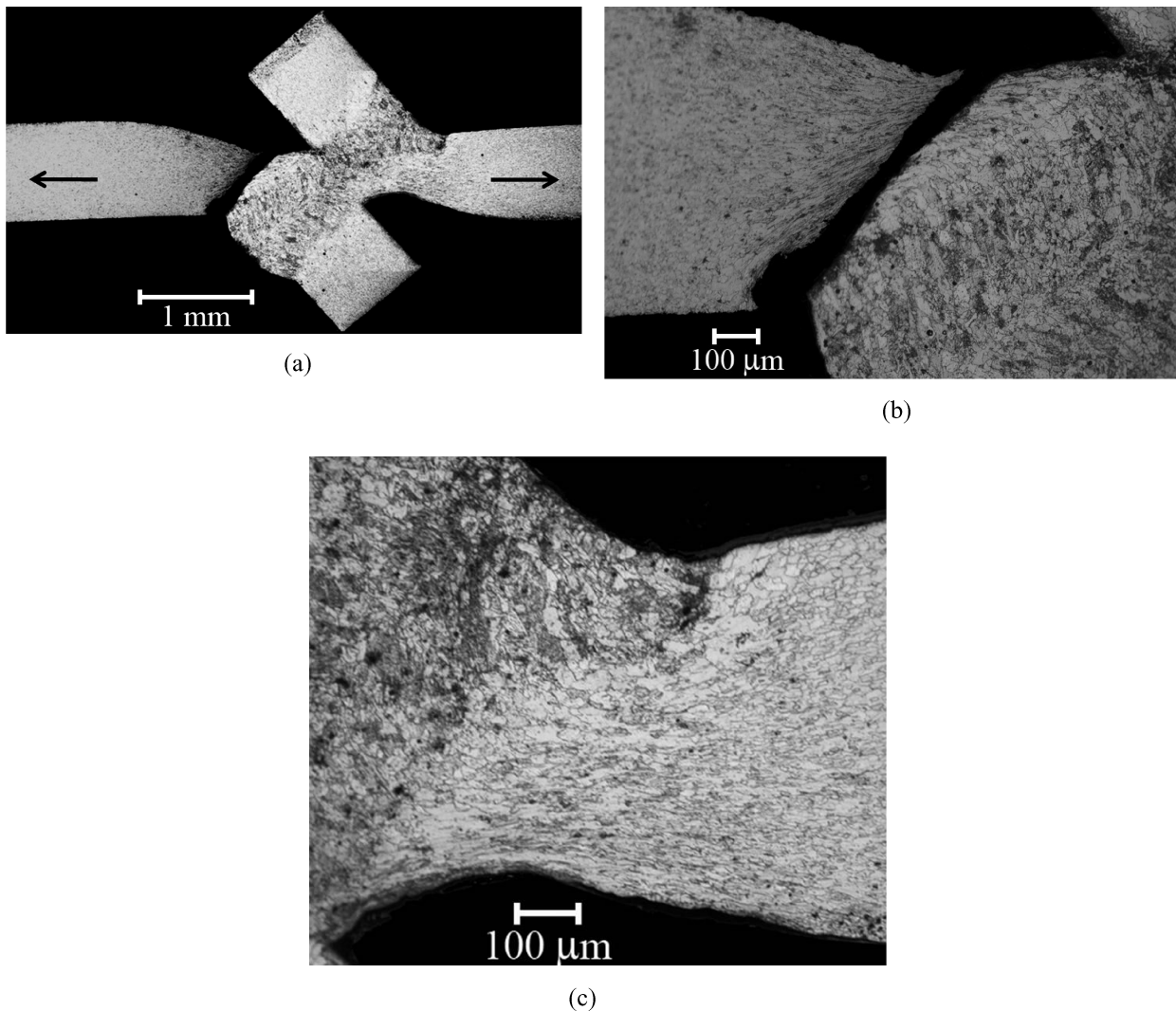
the pre-existing crack tip on the inner surface of the lower left sheet can also be observed and is marked in Fig. 7a. A close-up view of the region near the crack formation is provided as an insert in Fig. 7a. The weld rotation with respect to the loading direction is also visible from the figure. From the micrograph, it appears that this rotation causes the relatively rigid weld bead to compress the outer surface of the lower left sheet to create a notch. The notch further promotes the shear/necking instability and the final rupture of the lower left sheet.

Figure 7b shows a micrograph of the cross section of a completely failed weld. The thickness of the upper right sheet near the failure surfaces was noticeably reduced due to the necking. It is noted that the necking took place at a distance away from the pre-existing crack tips. Although the opening of the pre-existing crack tips is observed from the micrographs in Figs. 7a and b, the final failure was not initiated directly from these crack tips. The lower left sheet finally failed by ductile shear fracture as shown in Fig. 7b. This may seem to be a departure from the existing understanding of the fatigue failure of laser welds in which the failure is directly initiated from the pre-existing crack tip due to the stress and strain singularities based on the fracture mechanics approach.[9,10,16,19] Therefore, the failure mechanism of the necking/shear for laser welded lap joints of thin sheets under quasi-static loading conditions in the present study seems to be different from that under cyclic loading conditions.

Figure 8a shows an optical micrograph of the etched cross section of another completely failed weld. The opening of the pre-existing cracks and the sheet necking are visible in the micrograph. As shown in the figure, the non-load carrying sheets were cut for convenience of mounting the failed weld. As shown in the figure, the failure location is near the boundary of the base metal and the HAZ of the lower left load carrying sheet. The grains in this region are significantly stretched as seen in close-up views of the lower left sheet near the failure surface and the upper right sheet near the pre-existing crack tip in Figs. 8b and c, respectively.

In order to study the failure modes in the failed sheets, the failure surfaces of the separated sheets were examined under a scanning electron microscope. Figure 9a shows a scanning electron micrograph that gives an overview of the failure surface on the separated sheet side as indicated in Fig. 7b. The upper portion of the failure surface in Fig. 9a shows the stretch marks corresponding to the stretched inner surface of the lower sheet. The stretch marks suggest that this part of the sheet was subjected to tensile deformation and experienced significant plastic deformation. Note that the ratio of the width to the thickness is 8.6 for the specimens. The large ratio suggests that the majority of the weld was possibly subjected to plane strain loading conditions. Only a limited amount of

(a)

(b)

(c)

Fig. 8 (a) An optical micrograph of the etched cross section of a failed weld, and close-up views of (b) the lower left sheet near the failure surface and (c) the upper right sheet near the pre-existing crack tip (3% Nital solution used as the etchant).

necking in the transverse direction on both sides of the failure surface is shown in the figure. A close-up view of region I in Fig. 9a is shown in Fig. 9b. Three distinct regions A, B and C are identified from the scanning electron micrograph of the failure surface. Region A exhibits a fracture surface of large and small dimples. A close-up view of a portion of this region is shown in Fig. 9c. This portion of the failure surface corresponds to the crack initiation and growth. Region B exhibits a fracture surface with small elongated dimples. Region B of the failure surface indicates a shear dominant failure mode. A close-up view of a portion of the transition region between regions A and B is shown in Fig. 9d. Region C of the failure surface in Fig. 9a shows a flat and cleavage fracture surface. The cleavage fracture surface corresponds to the final stage of the separation of the weld joint due to the loss of the

load carrying capacity. A close-up view of a portion of the transition region between regions B and C is shown in Fig. 9e.

In a separate study,[16] it was observed that the fatigue failure in laser welded lap-shear specimens of HSLA steel sheets occurred due to the kinked crack growth from the pre-existing crack tip. The experimental observations in the present study indicate that the failure of laser welded lap-shear specimens under quasi-static loading conditions is driven by two distinct mechanisms that occur concurrently. One of the mechanisms involves the sheet necking/ thinning due to the combined axial and bending nature of the loading condition. The other mechanism is related to the weld rotation producing a notch in the HAZ of the lower left sheet adjacent to the weld bead protrusion due to the material inhomogeneity of the welded region and
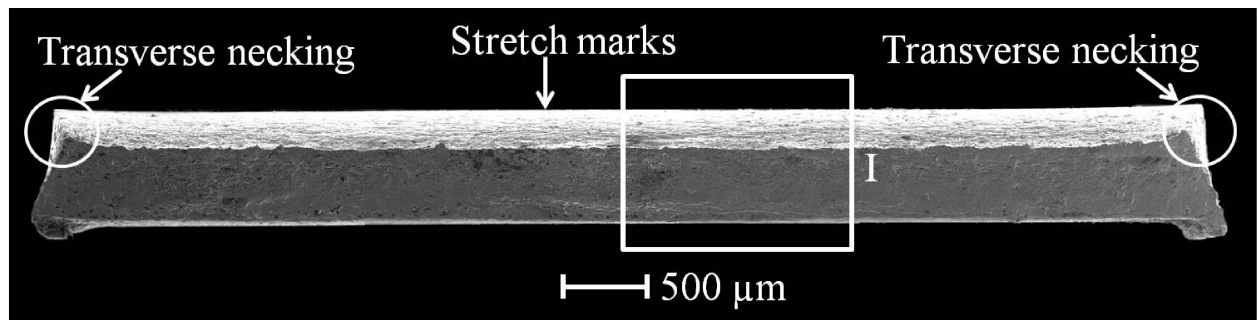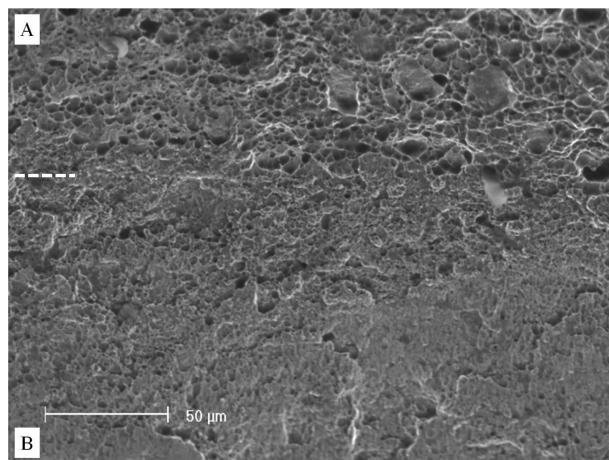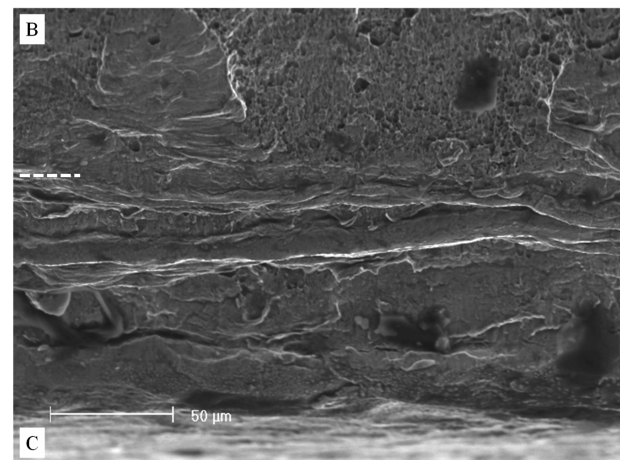
(a)
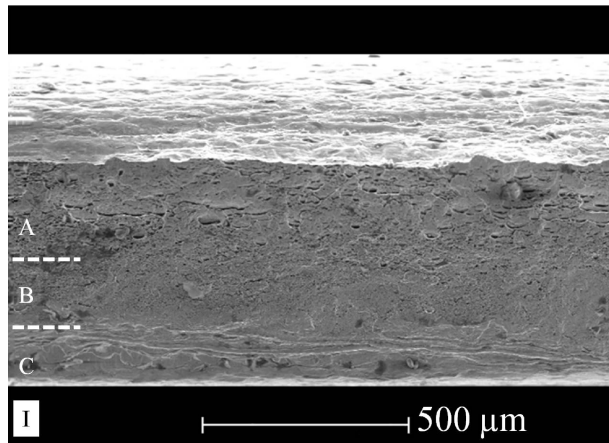
(b)
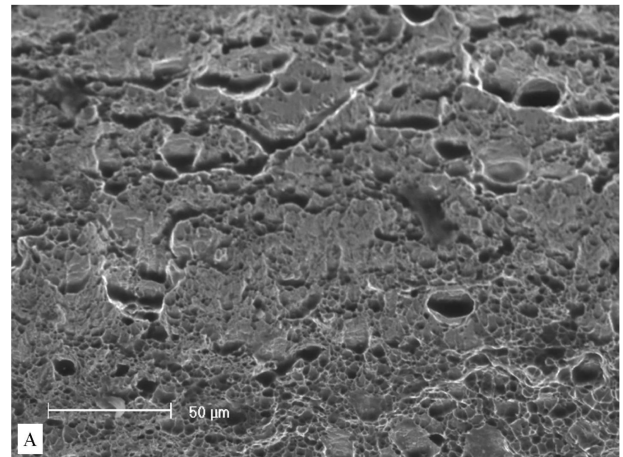
(c)

(d)

(e)

Fig. 9 (a) A scanning electron micrograph of the failure surface on the separated sheet side, (b) a close-up view of region I in (a), and close-up views of portions of (c) region A, (d) the transition region between regions A and B and (e) the transition region between regions B and C.

the geometry of the weld bead protrusion. The net area of the load carrying sheet to support the load is further reduced by the crack formation on the inner surface of the lower left sheet. The lower left sheet finally fails due to the loss of the load carrying capacity. The scanning electron micrographs of the failure surface shown in Figs. 9d and e indicate the presence of both small elongated dimples and cleavage surface corresponding to the final stage of the failure due to the loss of the load carrying capability of the sheet.

Table 3 The hardness values from indentation tests and the scaled initial yield stresses for the base metal, heat-affected zone (HAZ) and fusion zone for the 3-zone model

	Base metal	HAZ	Fusion zone
Vickers hardness	150	190	230
Yield stress σ_o (MPa)	315	400	484

Table 4 The hardness values from indentation tests and the scaled initial yield stresses for the base metal, heat-affected zone (HAZ) and fusion zone for the 6-zone model

	Base metal	HAZ 1	HAZ 2	Fusion 1	Fusion 2	Fusion 3
Vickers hardness	150	166	182	198	214	230
Yield stress σ_o (MPa)	315	349	382	416	450	484

The results of the finite element analyses of Lee et al.[14] are briefly reviewed here for completeness. Lee et al.[14] conducted finite element analyses with and without consideration of void nucleation and growth to investigate the failure mode of the laser welds in lap-shear specimens based on the experimental results reported here. They used non-homogenous 3-zone and 6-zone material models to more realistically represent the material behaviour in the base metal, HAZ and fusion zone. The stress–plastic strain curves for the material sections in the HAZ and fusion zone were estimated by scaling the stress–plastic strain curve of the base metal according to the hardness values of the different material sections of the HAZ and fusion zone. The assumed hardness values and the yield stresses of the material sections in the 3-zone and 6-zone models are listed in Tables 3 and 4, respectively. The detailed information on the 3-zone and 6-zone material model can be found in Lee et al.[14]

Figure 10a shows an optical micrograph of the etched cross section of the weld in a lap-shear specimen shown in Fig. 7a. The weld in Fig. 10a was subjected to the applied displacement of 1.95 mm prior to the final failure. Figures 10b and c show the deformed meshes near a weld in a lap-shear specimen at the applied displacement of 2.4 mm from the finite element analyses of Lee et al.[14] based on the 3-zone and 6-zone models, respectively. The necking of the two load carrying sheets is apparent in Figs. 10b and c. Figures 10b and c show that the plastic deformation concentrates in the base metal near the boundary of the base metal and the HAZ for both load carrying sheets. When Figs. 10b and c are compared, the deformed mesh of the 6-zone model near the crack tips is smoother than that of the 3-zone model. The details of the finite element

analyses and the selection of the material parameters can be found in Lee et al.[14] and are not reported here. It should be noted that in these finite element analyses, no failure criteria were adopted. Therefore, the finite element analyses can continue until a numerical instability takes place.

The Gurson's yield function was also adopted in the finite element analyses to identify the fracture initiation site near the weld in lap-shear specimens under quasi-static loading conditions. The location of the highest void volume fraction of the material elements from the finite element analysis based on the Gurson's yield function is indicated on the deformed mesh in Fig. 10c. This location corresponds to region *a* shown in the micrograph in Fig. 10a. The fracture surface with large dimples in Fig. 9c corresponds to region *a* in Fig. 10a. The creation of the artificial notch due to the buckling of the outer surface of the lower left sheet is shown in the deformed meshes in Figs. 10b and c. The creation of the notch from the finite element analyses agrees well with the experimental observation of a notch marked as *b* in the micrograph in Fig. 10a. In general, the deformed meshes based on the 3-zone and 6-zone models resemble the experimental observations shown in Fig. 10a. Although Figs. 10a and c correspond to different displacements, the general trend of the necking and the outer surface buckling of the lower left sheet can still be qualitatively correlated.

J INTEGRAL SOLUTIONS FOR 3-ZONE MATERIAL MODEL

In this section the $\mathcal{J}$ integral solutions obtained from the finite element analyses based on the 3-zone material model are used to explain the ductile failure mode observed in the experiment. Figure 11 shows a schematic of a crack and an arbitrary contour Γ surrounding the crack tip. As shown in the figure, a Cartesian coordinate system is centred at the crack tip. The $\mathcal{J}$ integral is defined as[20]

$$\mathcal{J} = \int_{\Gamma} \left(W n_x - T_i \frac{\partial u_i}{\partial x} \right) ds, \quad (i = x, y, z), \quad (1)$$

where Γ represents a counterclockwise contour from the lower crack face to the upper crack face, ds represents the differential arc length of the contour Γ, n_x represents the x component of the unit outward normal $\mathbf{n}$ to the differential arc length ds, T_i $(=\sigma_{ij} n_j)$ represents the components of the traction vector $\mathbf{T}$ on the differential arc length ds, and u_i represents the components of the displacement vector $\mathbf{u}$. In the above equation, the strain energy density W is defined as

$$W = \int_0^{\varepsilon_{ij}} \sigma_{ij} \, d\varepsilon_{ij}, \quad (i, j = x, y, z). \quad (2)$$

(a)

(b)

(c)
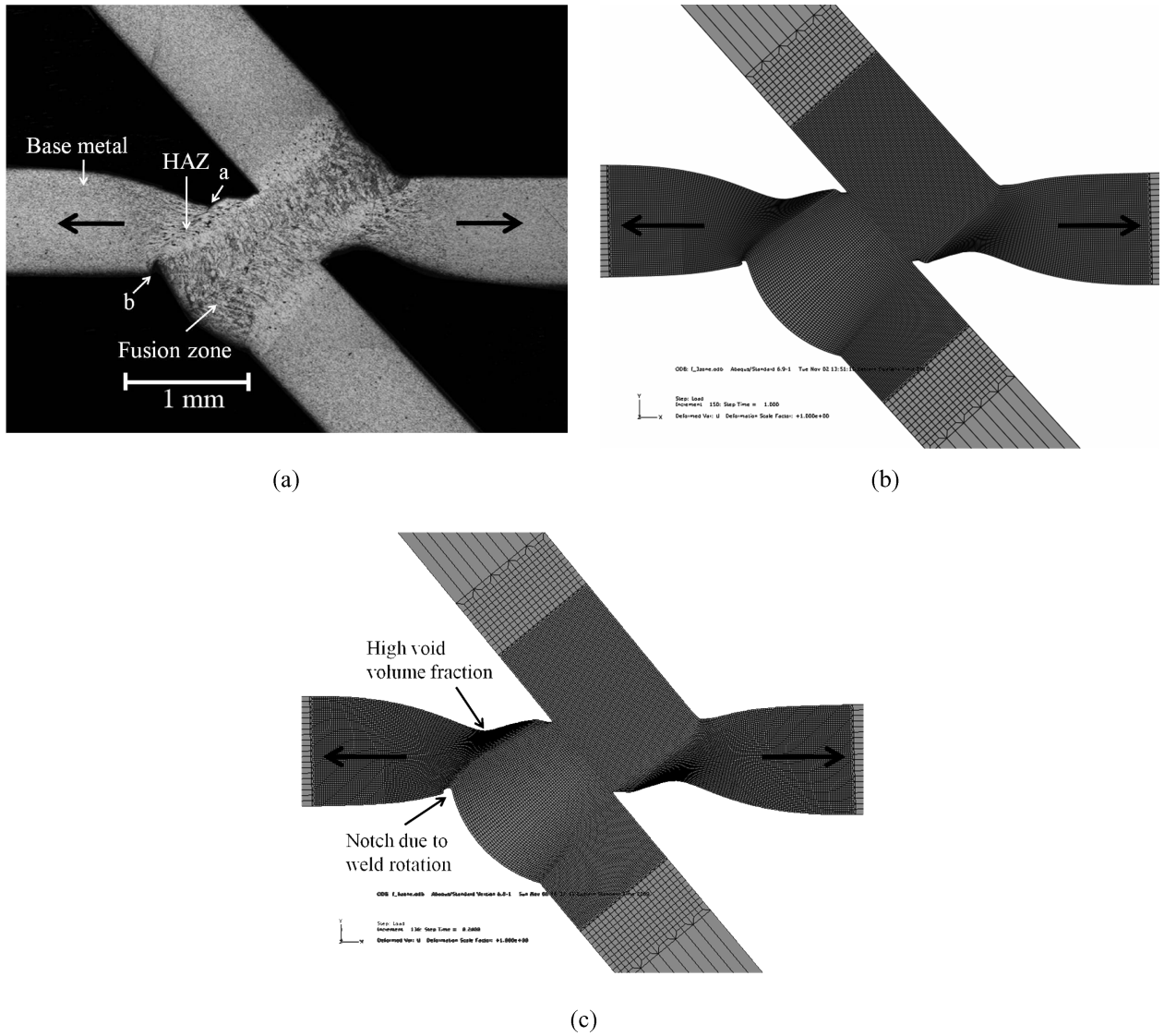
Fig. 10 (a) An optical micrograph of the etched cross section of a weld in a lap-shear specimen at the applied displacement of 1.95 mm prior to the final failure, and the deformed mesh near a weld in a lap-shear specimen at the applied displacement of 2.4 mm from the finite element analysis based on (b) the 3-zone model and (c) the 6-zone model.
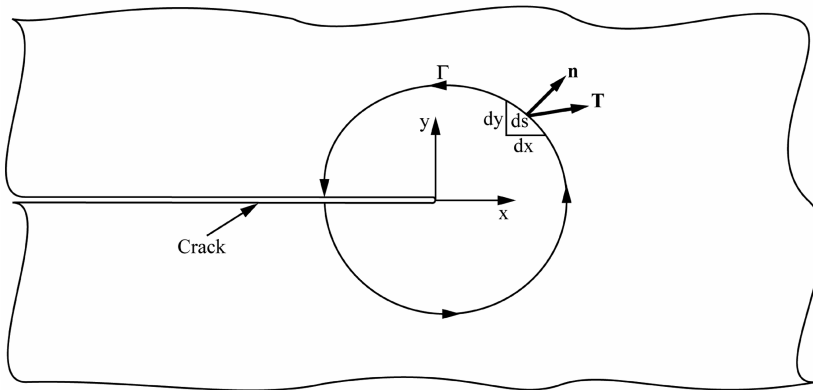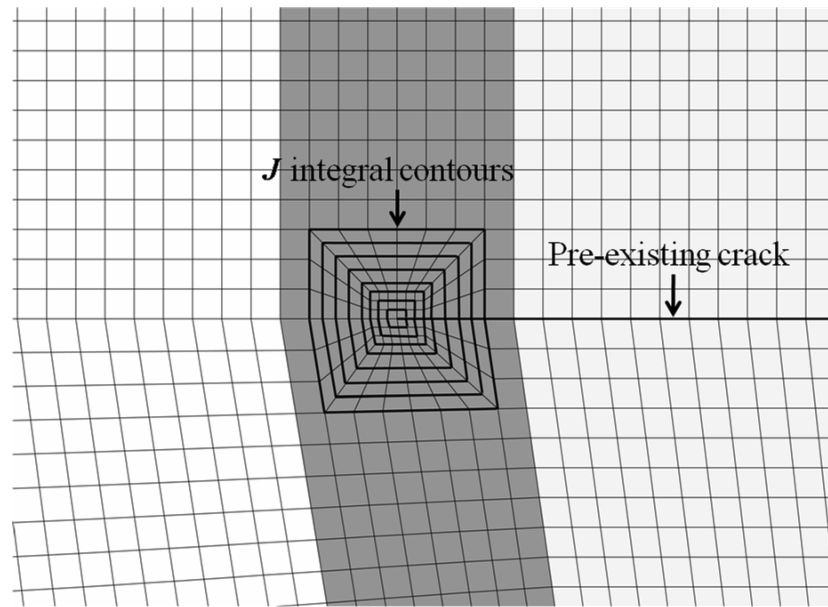

Fig. 11 A schematic of a crack and an arbitrary contour Γ surrounding the crack tip.
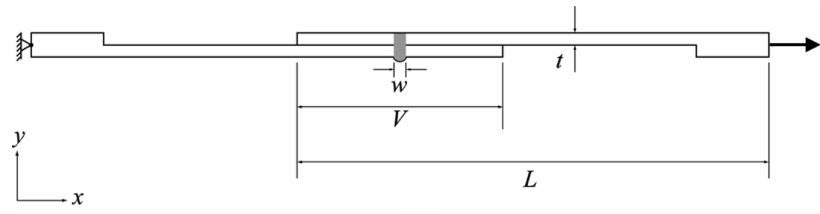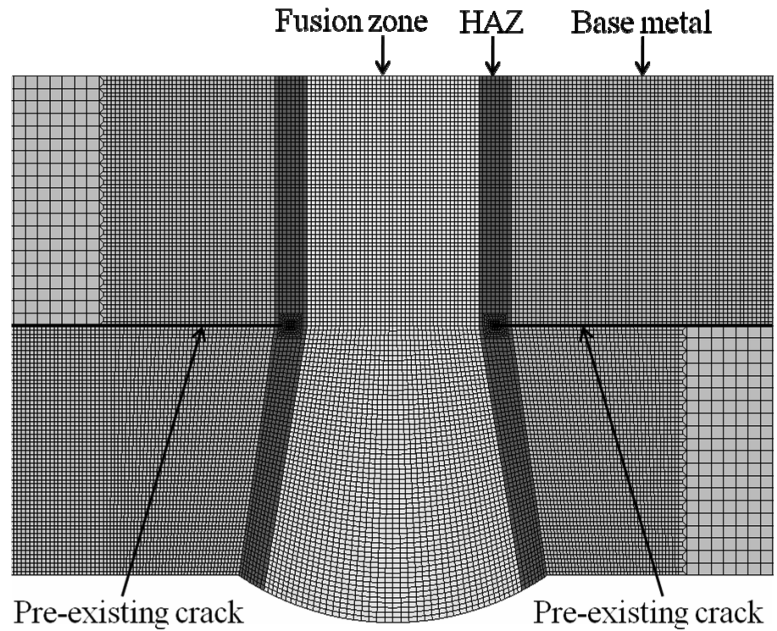
Fig. 12 (a) A schematic of a two-dimensional finite element model of a lap-shear specimen and the boundary conditions, (b) the finite element mesh near the weld and (c) a close-up view of the finite element mesh near the right pre-existing crack tip.

The $\mathcal{J}$ integral is path independent for a crack in a homogenous nonlinear elastic material. For elastic–plastic power-law strain hardening materials under proportional loading conditions, the $\mathcal{J}$ integral can be used to represent the singularity amplitude of the crack-tip stress and strain fields. Figure 12a shows a schematic of a two-dimensional finite element model of a lap-shear specimen and the boundary conditions. The Cartesian x-y coordinate system is also shown in the figure. The middle surface of the left edge is fixed whereas displacement in the $+x$ direction is applied at the middle surface of the right edge. The specimen has the length L, the overlap length V and the weld width w. Both the upper and lower sheets have the same thickness t. The two-dimensional plane-strain finite element model has the sheet thickness $t = 0.93$ mm, length $L = 82$ mm, overlap length $V = 30$ mm and weld width $w = 0.86$ mm between the two pre-existing crack tips. The width b of the central reduced width portion of the specimen is taken as 8 mm to calculate the applied force. First-order, plane strain, quadrilateral, reduced integration (CPE4R) elements are used in this model.

Figure 12b shows the finite element mesh near the weld based on the 3-zone material model of Lee *et al.*[14] for the ratio of the weld width to the sheet thickness, $w/t = 0.86$. As shown in the figure, there are three types of material zones: base metal, HAZ and fusion zone. A finer mesh is used near the pre-existing crack tips with the element size of about 4.75 μm. Figure 12c shows a close-up view of the mesh near the right pre-existing crack tip. A total of eight contours were assigned in the HAZ of the finite element model to obtain the $\mathcal{J}$ integral solutions. These contours are shown as thick lines surrounding the right pre-existing crack tip in Fig. 12c. Because all eight contours are in the HAZ which is homogenous, the $\mathcal{J}$ integral should be path independent and represents a fracture parameter of the crack tip under nearly proportional loading conditions. Note that near the crack tips in the HAZ, the grain size varies from several μm to about 30 μm as shown in Asim *et al.*[9] The $\mathcal{J}$ integral, instead of a local crack-tip parameter such as the crack-tip opening displacement or crack-tip opening angle, is selected here for the fracture parameter because the $\mathcal{J}$ integral is a macroscopic continuum path independent fracture parameter whereas the local crack-tip opening displacement or crack-tip opening angle is mesh dependent from finite element analyses.

The elastic modulus and the Poisson's ratio are taken as 206 GPa and 0.3, respectively, for the elastic material properties for the base metal, HAZ and fusion zone in the finite element analyses. The three different stress–plastic strain curves for the base metal, HAZ and fusion zone, scaled by the hardness values,[14] are adopted here. The hardness values and the scaled initial yield stresses for the base metal, HAZ and fusion zone are listed in Table 3. The scaled stress–plastic curves for the base metal, HAZ and
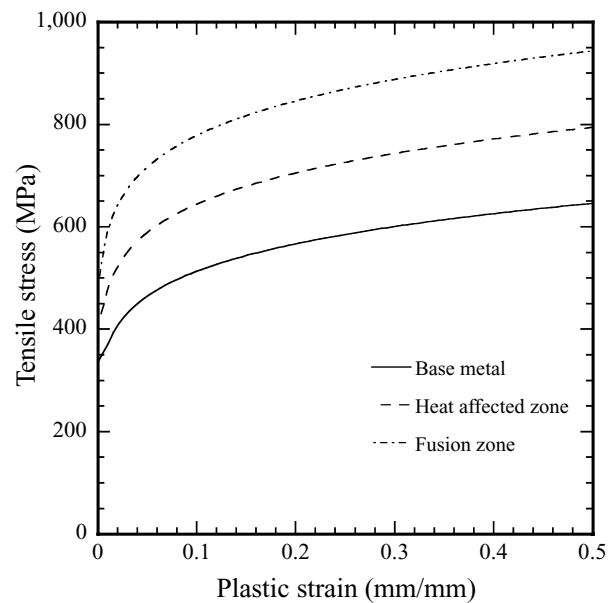

Fig. 13 The tensile stresses as functions of the plastic strain for the base metal, heat-affected and fusion zones used in the 3-zone finite element analysis.

fusion zone are shown in Fig. 13. The Mises yield function is adopted to describe the elastic–plastic behaviour of the material with the tensile stress–plastic strain curve used as the effective stress–plastic strain curve. The yield surface evolution is assumed to follow the isotropic hardening rule. It should also be noted that the residual stresses near the weld are not considered in this study due to the lack of quantitative information. Computations were performed using the commercial finite element code ABAQUS.[21]

The $\mathcal{J}$ integral contours are numbered 1 to 8, where contour 1 is closest to the tip and contour 8 is farthest away from the tip. The $\mathcal{J}$ integral solutions from the finite element analysis for contours 4 to 8 for the right pre-existing crack tip are plotted as functions of the normalized applied load in Fig. 14. The reference load $P_o (= \sigma_o b t)$ was used to normalize the applied load where σ_o is the yield stress of the base metal. It should be noted that the $\mathcal{J}$ integral solutions from the finite element analysis are higher for the right pre-existing crack tip as compared to those for the left pre-existing crack tip due to the presence of the weld bead protrusion on the lower surface of the weld. Therefore, the $\mathcal{J}$ integral solution for the right pre-existing crack tip is considered in this study because the fracture will be initiated from the right pre-existing crack tip when the $\mathcal{J}$ integral reaches a critical value. It should also be noted that the $\mathcal{J}$ integral is path independent for a crack in a homogenous nonlinear elastic material.[20] The maximum variation of the $\mathcal{J}$ integral solutions for contours 4 to 8 is less than 15% for a given load. However, the general trends of the solutions are quite consistent.
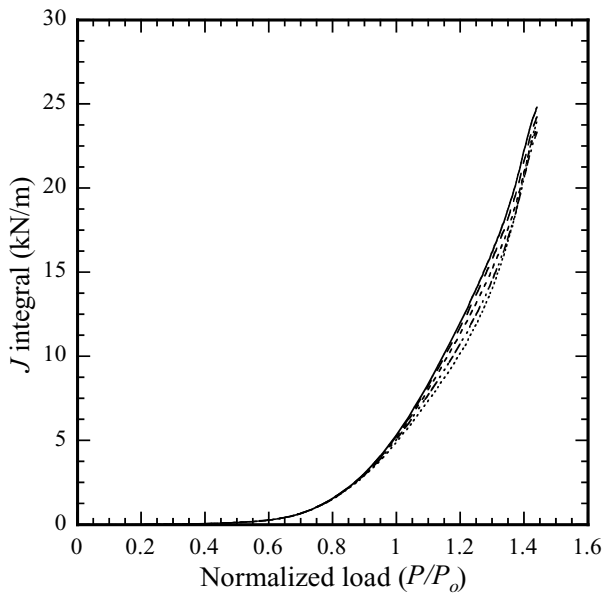
Fig. 14 The J integral solutions for contours 4 to 8 for the right pre-existing crack tip as functions of the normalized load from the finite element analysis.
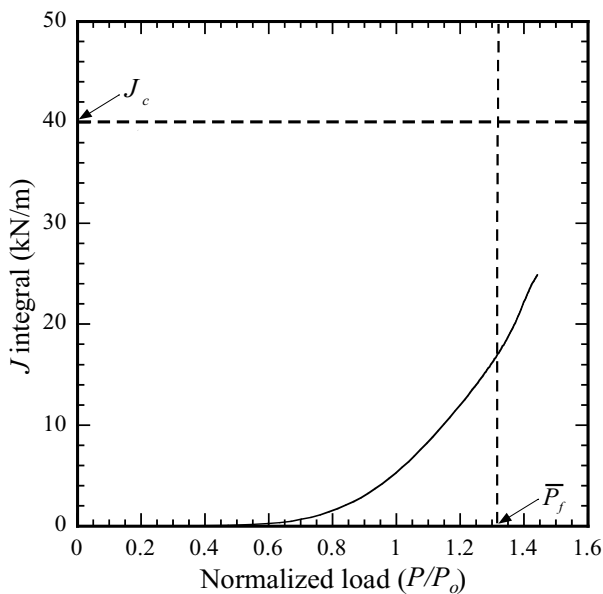

Fig. 15 The J integral solution for contour 8 for the right pre-existing crack tip as a function of the normalized load from the finite element analysis.

Figure 15 shows the J integral solution for contour 8 as a function of the normalized load from the finite element analysis. Figure 15 also shows the failure curves that can be used to predict the failure mode of the laser welds in lap-shear specimens. The vertical dashed line in Fig. 15 represents the failure load due to the plastic collapse or necking/shear as observed in the experiments. The nor-

malized failure load $\bar{P}_f$ can be defined as

$$\bar{P}_f = \frac{P_f}{P_o}, \tag{3}$$

where P_f is the failure load and P_o is a reference load. The failure load P_f can be estimated as

$$P_f = \sigma_u bt, \tag{4}$$

where σ_u is the tensile strength, b is the reduced specimen width and t is the sheet thickness. The reference load P_o is again defined as

$$P_o = \sigma_o bt. \tag{5}$$

Therefore,

$$\bar{P}_f = \frac{\sigma_u}{\sigma_o}. \tag{6}$$

For the given HSLA steel, $\bar{P}_f$ is 1.31 from the results of the tensile tests. This is in good agreement with the experimental results of the failure or maximum loads of the laser welds in lap-shear specimens. The horizontal dashed line in Fig. 15 represents the critical J_c of the HAZ in which the fracture initiation takes place at the pre-existing crack tip. Due to the unavailability of the actual critical J_c for the HAZ of the HSLA steel sheet under investigation, an average value of 40 kN/m for the fracture toughness of low carbon steels is selected as the critical J_c for the HAZ to demonstrate the use of the failure curves in the present study. Figure 15 shows that for the specimen with a sheet thickness of $t = 0.93$ mm, the weld is likely to fail in the plastic collapse or necking/shear failure mode as the applied load reaches the failure load P_f before reaching the critical J_c.

DISCUSSION ON THE EFFECTS OF SHEET THICKNESS ON FAILURE MODE

Ono *et al.*[10] reported failures of laser welds in the base metals of lap-shear specimens of thin steel sheets and correlated the weld strength to the tensile strength of the base metal. They also reported failures of laser welds in the welds and correlated the weld strength to the hardness of the weld. The failure mechanism of thin HSLA steel sheets under quasi-static loading conditions in the present study is observed to be the necking/shear in the base metal near the HAZ and the buckling of the lower left sheet, but a different failure mode dominated by fracture initiation from the pre-existing crack tip may be observed in welds of thicker sheets. In order to study the failure mode based on fracture initiation from the pre-existing crack tip and to evaluate the effect of sheet thickness on the failure mode, the J integral approach is adopted and discussed below.

$\mathcal{J}$ integral solutions for specimens with different thicknesses

In this study, the sheet thickness t in the finite element model is varied in order to investigate the effect of the sheet thickness on the $\mathcal{J}$ integral solutions and, in turn, on the failure mode of the laser welds in lap-shear specimens. It should be noted that the weld width, weld geometry and the material variation in the weld area can affect the failure mode of the weld as investigated by Lee *et al.*[14] Due to the unavailability of the actual welded specimens of different sheet thicknesses, all the dimensions of the weld and the specimen are scaled up proportionally by the sheet thickness in the finite element models in the present study. Therefore, the ratio of the weld width to the sheet thickness, $w/t = 0.86$, is kept the same for all finite element models with different thicknesses. The finite element models were scaled up by factors of 2, 3, 4 and 5 to represent the specimens with larger thicknesses. Therefore, five different thicknesses of t, $2t$, $3t$, $4t$ and $5t$, were used in the finite element models. Here, t represents the sheet thickness of the original lap-shear specimen and is equal to 0.93 mm.

Figure 16 shows the $\mathcal{J}$ integral solutions for contour 8 for the right pre-existing crack tips from the finite element analyses of the specimens with the sheet thicknesses of t, $2t$, $3t$, $4t$ and $5t$. The $\mathcal{J}$ integral solutions are plotted as functions of the normalized applied load for the specimens with the different thicknesses. Figure 16 shows
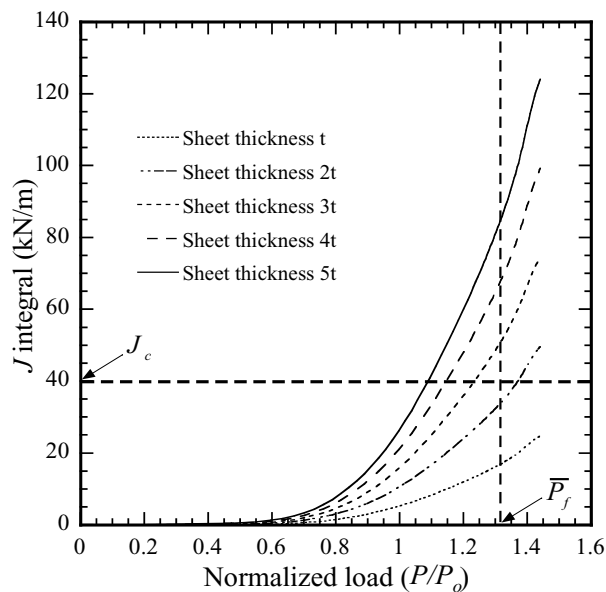
that the $\mathcal{J}$ integral solutions for a given normalized applied load increase as the sheet thickness increases. The failure curves in Fig. 16 can be used to predict the failure mode of the laser welds in these lap-shear specimens. The vertical dashed line in Fig. 16 represents the normalized failure load due to plastic collapse or necking/shear. The horizontal dashed line in Fig. 16 represents the critical $\mathcal{J}_c$ which is taken as 40 kN/m for the weld in the present study. For the specimens with the sheet thicknesses of t and $2t$, the plastic collapse or the necking/shear failure loads are reached before the critical $\mathcal{J}_c$ is reached. For the specimens with the sheet thicknesses of $3t$, $4t$ and $5t$, the critical $\mathcal{J}_c$ is met before the plastic collapse failure loads are reached. A critical thickness $t_c = 2.22$ mm can be determined for the given critical $\mathcal{J}_c$ of 40 kN/m and normalized failure load $\bar{P}_f$ of 1.31 for the transition of the failure mode from the plastic collapse to the fracture initiation from the right pre-existing crack tip. This critical thickness depends on the critical $\mathcal{J}_c$ of the HAZ and the tensile strength of the base metal. If the welding process causes a reduction of the critical $\mathcal{J}_c$ of the HAZ, then a failure by fracture initiation from the right pre-existing crack tip is more likely to occur for thinner sheets. Conversely, a lower tensile strength of the base metal can cause a failure by plastic collapse or necking/shear for thicker sheets. It should be noted that the effect of the weld width is not investigated in this study. Laser welds normally have a very small weld width. However, a larger ratio of the weld width to the sheet thickness is needed to prevent any interfacial fracture through the weld.

It should be noted that Ono *et al.*[10] reported that for the lap-shear specimens of thin steel sheets used in their investigation with sheet thicknesses above 1.2 mm, the fracture occurred in the weld metal instead of the base metal as observed in the specimens with thinner sheets. This observation of the change of failure location of the welds based on sheet thickness motivates the present study and can be explained based on the use of the failure curves in Figs. 15 and 16. However, a more detailed experimental investigation for welds with different sheet thicknesses and for other types of metals can be conducted to verify the concept of the failure curves presented here.

Fig. 16 The $\mathcal{J}$ integral solutions for contour 8 for the right pre-existing crack tip as functions of the normalized load from the finite element analyses of the specimens with the sheet thicknesses of t, $2t$, $3t$, $4t$ and $5t$.

Scalability of the $\mathcal{J}$ integral solutions

As shown in Fig. 16, for a given normalized load, the $\mathcal{J}$ integrals are larger for specimens with larger thicknesses. When the thickness t and the weld width w are the most important length parameters for the homogenous material model of the lap-shear specimen with a weld,[14] the $\mathcal{J}$ integral should be scaled to the thickness for both linear elastic and pure power-law hardening material for a fixed ratio of w/t. In order to determine if the scalability of the $\mathcal{J}$ integral by the sheet thickness is possible for the
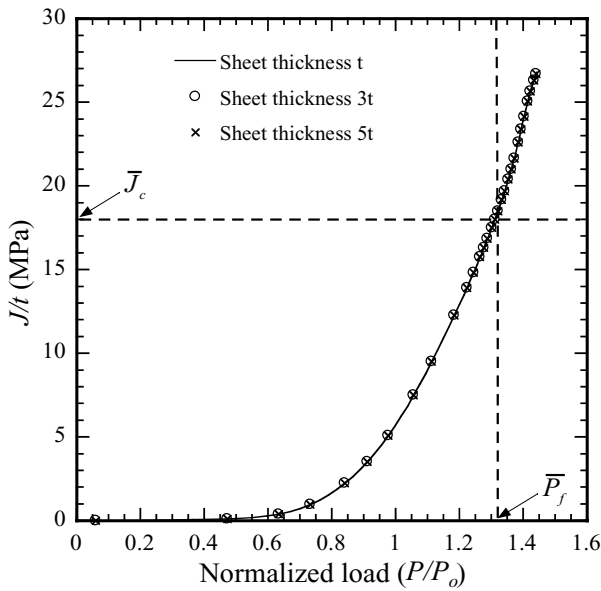
Fig. 17 The values of the normalized $\bar{J}(=\bar{J}/t)$ for contour 8 for the right pre-existing crack tips as functions of the normalized load from the finite element analyses of the specimens with the sheet thicknesses of t, $3t$ and $5t$.

non-homogenous 3-zone model, the J integral solutions normalized by the sheet thickness t are plotted as functions of the normalized load in Fig. 17. Figure 17 shows the values of the normalized J integral, $\bar{J}(=J/t)$, for contour 8 for the right pre-existing crack tips from the finite element analyses of the specimens with the sheet thicknesses of t, $3t$ and $5t$. Figure 17 shows that the normalized J integral solutions collapse into a single curve. This indicates the scalability of the J integral by the sheet thickness t for the specimens with different thicknesses for the given ratio of $w/t = 0.86$.

For pure power-law hardening homogeneous materials, the J integral should be scaled by the only significant length dimension of the geometry of interest.[22] For the laser welds in lap-shear specimens, when the weld width is significantly larger than the thickness, the thickness becomes the only significant length dimension according to the beam bending theory. For the given ratio $w/t = 0.86$, the stress intensity factor solutions derived from the beam bending theory are reasonably close to the actual stress intensity factor solutions obtained from the finite element analysis for linear elastic homogeneous materials.[8] This suggests that the beam bending theory may be approximately applicable to laser welds in lap-shear specimens for the given ratio $w/t = 0.86$ under elastic–plastic deformation. For pure power-law hardening homogeneous materials, it can be shown that the J integral should be scaled by the thickness for the two-strip model of Sripichai et al.[8] For the 3-zone finite element model, the J inte-

gral for the crack tip in the HAZ should depend on the sheet thickness, the width of the HAZ, the width of the fusion zone, the remaining ligament between the crack tip and the fusion zone and the material variation in the weld zone. When the weld geometry is scaled up proportionally with respect to the sheet thickness while the material variation is kept to be the same, the J integrals is apparently scaled by the sheet thickness as indicated in Fig. 17.

The failure curve and the scaled J integral curves for a sheet of unit thickness can be used to conveniently determine the critical sheet thickness for the transition of the failure mode. As a demonstration, the value $\bar{\bar{J}}_c = J_c/t$ obtained from the normalized J integral curve in Fig. 17 for the normalized failure load $\bar{P}_f$ of 1.31 is about 18 MPa as shown in the figure. Dividing the selected fracture toughness of 40 kN/m by this value of $\bar{\bar{J}}_c$ gives a value of 2.22 mm for the critical sheet thickness t_c as mentioned earlier.

Based on the earlier discussion, the failure load P_f can be expressed as

$$P_f = \sigma_u b t \text{ for } t \leq t_c, \tag{7}$$

$$P_f = \sigma_o b t \bar{P}(\bar{\bar{J}}_c) \text{ for } t > t_c, \tag{8}$$

where $\bar{P}(\bar{\bar{J}}_c)$ represents the normalized load $\bar{P}$ as a function of $\bar{\bar{J}}_c$. Figure 18 shows the plots of the failure load P_f as a function of the sheet thickness t based on Eqs (7) and (8) for specimens with different thicknesses. Different J_c values of 30, 40 and 50 kN/m are used to plot three different curves representing Eq. (8). Figure 18 shows that for sheet thicknesses smaller than the critical sheet thickness
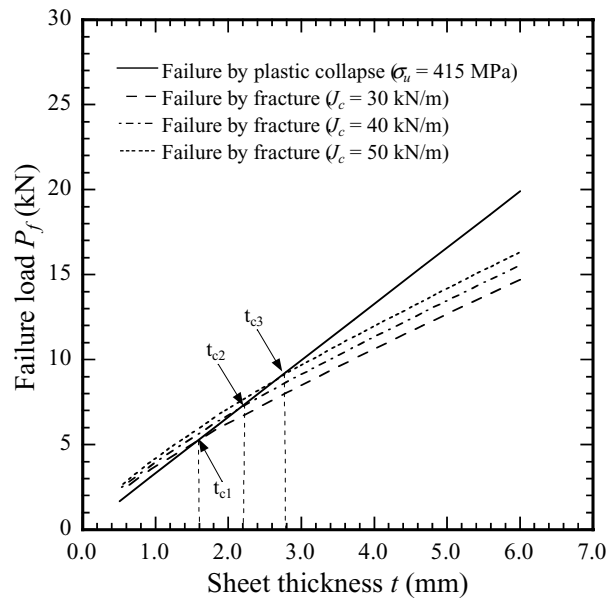

Fig. 18 The values of the failure load P_f as functions of the sheet thickness t for different values of J_c.

t_{c1} for $\mathcal{J}_c = 30$ kN/m, t_{c2} for $\mathcal{J}_c = 40$ kN/m and t_{c3} for $\mathcal{J}_c = 50$ kN/m, the failure load based on the plastic collapse failure mode is lower than the failure load required to initiate fracture from the pre-existing crack tips. For sheet thicknesses larger than the critical sheet thickness t_{c1} for $\mathcal{J}_c = 30$ kN/m, t_{c2} for $\mathcal{J}_c = 40$ kN/m and t_{c3} for $\mathcal{J}_c = 50$ kN/m, the failure load to cause fracture initiation is smaller than the failure load based on the plastic collapse failure mode, and the failure is likely to occur by fracture initiation from the pre-existing crack tips. It should be noted that the critical sheet thickness t_c decreases as the critical $\mathcal{J}_c$ decreases. This indicates that for a weld with a lower critical $\mathcal{J}_c$, the failure by fracture initiation can occur at a smaller thickness. In summary, the failure criteria of welds based on the plastic collapse failure mode should be used cautiously for welds of thicker sheets due to possible lower failure loads due to the fracture initiation from the pre-existing crack tips.

CONCLUSIONS

In this paper, the failure mode of laser welds in lap-shear specimens of non-galvanized SAE J2340 300Y HSLA steel sheets under quasi-static loading conditions is examined based on experimental observations and finite element analyses. Laser welded lap-shear specimens with reduced cross sections were made. Optical micrographs of the cross sections of the welds in the specimens before and after tests are examined to understand the microstructure and failure mode of the welds. Micro-hardness tests were also conducted to provide an assessment of the mechanical properties in the base metal, HAZ and fusion zone. The micrographs indicate that the weld failure appears to be initiated from the base metal near the boundary of the base metal and the HAZ at a distance away from the pre-existing crack tip, and the specimens fail due to the necking/shear of the lower left load carrying sheets. Finite element analyses based on non-homogenous multizone material models were conducted to model the ductile necking/shear failure and to obtain the $\mathcal{J}$ integral solutions for the pre-existing cracks. The results of the finite element analyses are used to explain the ductile failure initiation sites and the necking/shear of the lower left load carrying sheets. The $\mathcal{J}$ integral solutions obtained from the finite element analyses based on the 3-zone finite element model indicate that the $\mathcal{J}$ integral for the pre-existing cracks at the failure loads are low compared to the fracture toughness and the specimens should fail in a plastic collapse or necking/shear mode. The effects of the sheet thickness on the failure mode were then investigated for laser welds with a fixed ratio of the weld width to the thickness. For the given non-homogenous material model, the $\mathcal{J}$ integral solutions appear to be scaled by the sheet thickness. With consideration of the plastic collapse failure mode and fracture initiation failure mode, a critical thickness can be obtained for the transition of the plastic collapse or necking/shear failure mode to the fracture initiation failure mode. Finally, the failure load is expressed as a function of the sheet thickness according to the governing equations based on the two failure modes. The results demonstrate that the failure mode of welds of thin sheets depends on the sheet thickness, ductility of the base metal and fracture toughness of the HAZ. Therefore, failure criteria based on either the plastic collapse failure mode or the fracture initiation failure mode should be used cautiously for welds of thin sheets.

Acknowledgements

REFERENCES

1 Hsu, C. and Albright, C. E. (1991) Fatigue analysis of laser welded lap joints. *Eng. Fract. Mech.* **39**, 575–580.
2 Wang, P. C. and Ewing, K. M. (1991) A comparison of fatigue strengths: laser beam vs. resistance spot welds. *Weld. J.* **70**, 43–47.
3 Flavenot, J. F., Deville, J. P., Diboine, A., Cantello, M. and Gobbi, S. L. (1993) Fatigue resistance of laser welded lap joints of steel sheets. *Weld. World* **31**, 12–15.
4 Wang, P. C. and Ewing, K. M. (1994) Effect of process parameters on the fatigue strength of laser beam welds. *J. Laser App.* **6**, 14–22.
5 Terasaki, T., Sobue, T. and Kitamura, T. (2001) Study of fatigue strength of laser welded lap joint. *Q. J. Japan Weld. Soc.* **19**, 507–512.
6 Kaitanov, A. Y., Ozersky, A. D., Zabelin, A. M. and Kislov, V. S. (2002) Static and fatigue strengths of laser welded overlap joints with controlled penetration. *Proc. SPIE* **4644**, 116–126.
7 Cho, S. K., Yang, Y. S., Son, K. J. and Kim, J. Y. (2004) Fatigue strength in laser welding of the lap joint. *Finite Elem. Anal. Des.* **40**, 1059–1070.
8 Sripichai, K., Asim, K. and Pan J. (2011) Stress intensity factor solutions for estimation of fatigue lives of laser welds in lap-shear specimens. *Eng. Fract. Mech.* **78**, 1424–1440.
9 Asim, K., Sripichai, K. and Pan, J. (2011) Fatigue behavior of laser welds in lap-shear specimens of high strength low alloy steel sheets. Submitted for publication in *Int. J. Fatigue*.
10 Ono, M., Kabasawa, M. and Omura, M. (1997) Static and fatigue strength of laser-welded lap joints in thin steel sheet. *Weld. Int.* **11**, 462–467.
11 Chien, W. Y., Friedman, P. A. and Pan, J. (2003) Failure prediction of aluminum laser-welded blanks. *Int. J. Damage Mech.* **12**, 193–223.
12 Taban, E., Deleu, E., Dhooge, A. and Kaluc, E. (2009) Laser welding of modified 12% Cr stainless steel: strength, fatigue,

toughness, microstructure and corrosion properties. *Mater. Des.* **30,** 1193–1200.

13 Casavola, C., Pappalettere, C. and Tattoli, F. (2009) Experimental and numerical study of static and fatigue properties of titanium alloy welded joints. *Mech. Mater.* **41,** 231–243.

14 Lee, J., Asim, K. and Pan, J. (2011) Modeling of failure mode of laser welds in lap-shear specimens of HSLA steel sheets. *Eng. Fract. Mech.* **78,** 374–396.

15 Anand, D., Chen, D. L., Bhole, S. D., Anderychuk, P. and Bourdeau, G. (2006) Fatigue behavior of tailor (laser)-welded blanks for automotive applications. *Mater. Sci. Eng.* **A 420,** 199–207.

16 Sripichai, K., Asim, K., Jo, W. H., Pan, J. and Li, M. (2009) Fatigue behavior of laser welds in lap-shear specimens of high strength low alloy (HSLA) steels. SAE Tech. Paper No. 2009–01-0028. Society of Automotive Engineers, Warrendale, PA.

17 Mei, L., Chen, G., Jin, X., Zhang, Y. and Wu, Q. (2009) Research on laser welding of high strength galvanized automobile steel sheets. *Optics Lasers Eng.* **47,** 1117–1124.

18 Radaj, D., Zhaoyun, Z. and Möhrmann, W. (1990) Local stress parameters at the weld spot of various specimens. *Eng. Fract. Mech.* **37,** 933–951.

19 Wang, P. C. (1995) Fracture mechanics parameter for the fatigue resistance of laser welds. *Int. J. Fatigue* **17,** 25–34.

20 Rice, J. R. (1968) A path independent integral and the approximate analysis of strain concentration by notches and cracks. *J. App. Mech.* **35,** 379–386.

21 ABAQUS v6.7 User Manual (2007) SIMULIA. Providence, RI.

22 Wang, Y. and Pan, J. (1999) Development of a multiaxial fatigue theory by considering constraint effects on small mixed mode cracks. *Int. J. Solids Struct.* **36,** 4543–4562.